Lithium Insertion in Channel-Structured β-$AgVO_3$: *In Situ* Raman Study and Computer Simulation

Qiaoliang Bao,[†,‡,⊥] Shujuan Bao,[†,⊥] Chang Ming Li,[*,†] Xiang Qi,[‡] Chunxu Pan,[*,‡] Jianfeng Zang,[§] Weiliang Wang,[†,||] and Ding Yuan Tang[§]

School of Chemical and Biomedical Engineering and Center for Advanced Bionanosystems, Nanyang Technological University, Singapore 639798, Singapore; Department of Physics and Key Laboratory of Acoustic and Photonic Materials and Devices of Ministry of Education, Wuhan University, Wuhan 430072, China; School of Electrical and Electronic Engineering and Center for Advanced Bionanosystems, Nanyang Technological University, Singapore 639798, Singapore; and State Key Lab of Optoelectronic Materials and Technology, School of Physics and Engineering, Sun Yat-Sen (Zhongshan) University, Guangzhou 510275, People's Republic of China

Received June 29, 2007. Revised Manuscript Received September 5, 2007

Lithium insertion is the fundamental electrochemical process of rechargeable lithium batteries. We report here *in situ* Raman and atomistic simulation studies of the lithium insertion process in β-$AgVO_3$ nanowired structure material. Key issues of the process relate to structural variations and lithium migration pathways in the β-$AgVO_3$. The simulation model shows good agreement with the experimental results. It indicates that the lithium insertion can be divided into three steps. The reduction sites at each step in the β-$AgVO_3$ lattice are confirmed: the most favorable reduction sites at higher potential are V1/V4; at medium potential, Ag2/Ag3 are reduced and substituted; after that Li^+ ion reduces V2/V3/Ag4 and further reduces V1/V4. The migration pathways of Li^+ ions in β-$AgVO_3$ are proposed for the first time. Our discovery would help us to greatly understand the deep insight of the Li^+ insertion process in lithium batteries.

1. Introduction

Silver vanadium oxides (SVO) are excellent potential battery materials for advanced biomedical devices and predominant power sources for implantable cardioverter defibrillators.[1–5] They have prominent advantages such as high power density, high energy density, and long-term stability due to their layered structure and excellent reaction kinetics for attractive battery materials.[6–8] In the past several decades, great efforts have been paid on the synthesis and characterization, phase separation and structural analyses, and electrochemical reactivity of SVO. Recently, nanoarchitectures have been introduced into the research to tailor SVO nanostructure for large specific surface areas and short diffusion paths.[7–11] This provides an ideal template for structural studies of lithium batteries. In addition, Li^+ storage mechanisms of bulk materials might not occur as the size scale decreases, and the structural changes might be more sensitive to Li^+ insertion for nanostructured SVO. Up to now, even though lots of various experimental data on SVO are available, the knowledge about the structural variations of nanoscale SVO in the Li^+ electroinsertion process is not clear. It is known that the electrochemical performance depends on the nature and amplitude of the structural changes induced by lithium incorporation. From the industrial point of view, it is of great importance to understand the structural variations of SVO so as to improve the electrochemical properties, i.e., to maintain and control the voltage to a given value of functioning.

X-ray diffraction (XRD) is broadly used for structural identification of SVO, with which the multiple phases of SVO[9–13] can be observed by indexing the powder pattern, and an *in situ* XRD is developed to investigate the phase transition of cathode materials.[14–16] However, XRD mea-

* To whom correspondence should be addressed: e-mail ecmli@ntu.edu.sg or cxpan@whu.edu.cn; Tel 65-6790-4485; Fax 65-6790-4485.
† School of Chemical and Biomedical Engineering, Nanyang Technological University.
‡ Department of Physics, Wuhan University.
§ School of Electrical and Electronic Engineering, Nanyang Technological University.
|| School of Physics and Engineering, Sun Yat-Sen (Zhongshan) University.
⊥ These authors contributed equally to this work.

(1) Takeuchi, K. J.; Marschilok, A. C.; Davis, S. M.; Leising, R. A.; Takeuchi, E. S. *Coord. Chem. Rev.* **2001**, *219*, 283.
(2) Takeuchi, E. S.; Leising, R. A. *MRS Bull.* **2002**, *27*, 624.
(3) Takeuchi, K. J.; Leising, R. A.; Palazzo, M. J.; Marschilok, A. C.; Takeuchi, E. S. *J. Power Sources* **2003**, *119*, 973.
(4) Brodd, R. J.; Bullock, K. R.; Leising, R. A.; Middaugh, R. L.; Miller, J. R.; Takeuchi, E. *J. Electrochem. Soc.* **2004**, *151*, K1.
(5) Whittingham, M. S. *Chem. Rev.* **2004**, *104*, 4271.
(6) Sorensen, E. M.; Izumi, H. K.; Vaughey, J. T.; Stern, C. L.; Poeppelmeier, K. R. *J. Am. Chem. Soc.* **2005**, *127*, 6347.
(7) Shen, G. Z.; Chen, D. *J. Am. Chem. Soc.* **2006**, *128*, 11762.
(8) Zhang, S. Y.; Li, W. Y.; Li, C. S.; Chen, J. *J. Phys. Chem. B* **2006**, *110*, 24855.
(9) Liu, Y.; Zhang, Y. G.; Hu, Y. G.; Qian, Y. T. *Chem. Lett.* **2005**, *34*, 146.
(10) Sharma, S.; Panthofer, M.; Jansen, M.; Ramanan, A. *Mater. Chem. Phys.* **2005**, *91*, 257.
(11) Liu, S. W.; Wang, W. Z.; Zhou, L.; Zhang, L. S. *J. Cryst. Growth* **2006**, *293*, 404.
(12) Kittaka, S.; Matsuno, K.; Akashi, H. *J. Solid State Chem.* **1999**, *142*, 360.
(13) Kittaka, S.; Nishida, S.; Iwashita, T.; Ohtani, T. *J. Solid State Chem.* **2002**, *164*, 144.
(14) Gustafsson, T.; Thomas, J. O.; Koksbang, R.; Farrington, G. C. *Electrochim. Acta* **1992**, *37*, 1639.

10.1021/cm071728i CCC: $37.00
Published on Web 11/03/2007

surements give only limited information on the lithium site in the crystal structure. By contrast, Raman spectroscopy is very sensitive to the symmetry of structure and structural variation near the surface region and particularly suitable for the molecular-level investigation of intercalation/deintercalation processes. Recently, *in situ* Raman spectroscopy has been used extensively to study the electrochemical insertion of Li^+ ions of cathode materials such as manganese oxides,[17–19] cobalt oxide,[20] vanadium pentoxide,[21,22] graphite,[23–25] and carbon nanotubes.[26,27] To the best of our knowledge, there is no report on applying an *in situ* Raman spectroscopy method to real-time monitor lithium insertion in β-$AgVO_3$. In addition, Raman spectra of crystalline bulk $AgVO_3$ are only reported in a recent literature by Tian et al.[28] even though SVO has been studied for many decades.[1] However, the phase and space group of bulk $AgVO_3$ are not assigned in the literature.[28]

We have reported a new approach to synthesize a novel channel-structured β-$AgVO_3$.[29] In present work, an *in situ* Raman spectroscopy method was employed to evaluate the insertion behavior of Li^+ in this nanostructured β-$AgVO_3$ for the first time. We report here not only the Raman spectra of crystalline β-$AgVO_3$ nanowires and corresponding vibrational modes but also the further studies of the whole process of Li^+ insertion in terms of the Raman spectra. Through these studies, we discovered the structural variation of electrode materials and the migration of inserted Li^+ from the *in situ* Raman spectra data and the analysis of atomistic simulation.

2. Experimental Section

2.1. Sample Preparation. The channel-structured β-$AgVO_3$ material was prepared by a hydrothermal method described in our early report.[28] In a typical synthesis procedure, a certain amount of $AgNO_3$ and NH_4VO_3 was dissolved into deionized water (80 mL) under ultrasonication. After 20 min ultrasonic reaction, the resulting mixture was transferred into a Teflon-lined stainless steel autoclave. Then the autoclave was sealed and heated to 180 °C for 3 h and 250 °C for another 9 h. The system was then cooled naturally to room temperature. The collected products after filtration were washed with deionized water and dried at 55 °C overnight. For the preparation of working electrode, a thick slurry was prepared by mixing the products with 5% ploytetrafluoroethylene (PTFE) and then pasted to a nickel mesh current collector (10×10 mm^2), followed by compressing and drying to obtain an electrode sheet.

2.2. *In Situ* Raman Studies. *In situ* Raman studies of the structural variation of electrode materials were carried out by a setup with an integrated confocal Raman microscope system (CRM 200, WITec, Germany) and an electrochemical workstation (CHI 660B, CH Instruments, Austin, TX). The Raman system was equipped with an Ar^+ laser (LASOS, LGN7812) having an excitation source at 488 nm and a charge coupled device (CCD) detector. The highest grating was adopted to reach a resolution of less than 2 cm^{-1}. Electrochemical measurements were performed using a three-electrode arrangement, including working electrode, platinum counter electrode, and Ag wire reference electrode. The electrolyte solution was acetonitrile containing 1 M $LiClO_4$ and 0.1 M tetrabutylammonium hexafluorophosphate (Bu_4NPF_6). The 50× objective lens of the microscope was used to focus the laser beam (~15 mW) on the thin film SVO electrode immersed in the electrolyte solution. For cyclic voltammetric (CV) experiments, the first cycle of discharge/charge voltammogram was recorded, and individual *in situ* Raman spectra were acquired while scanning the potential at 5 mV/s with an integration time of 20 s, therefore representing an average sample interval of over 100 mV. All measurements were carried out at room temperature (22 ± 2 °C).

3. Atomistic Simulation

An atomistic simulation method has been reported by using the GULP code developed by Gale.[30,31] This approach employs well-established atomistic modeling techniques and has been applied successfully to study a number of functional oxides and lithium battery materials such as V_2O_5,[32] TiO_2,[33] $LiMn_2O_4$,[34,35] and $LiFePO_4$.[36] The calculations are based on energy minimization procedures, with modeling of lattice defects performed using the two-region Mott–Littleton methodology,[37] which are described in detail in the literature.[30,31] The method can quickly and easily generate accurate structures and a wide range of physical properties of these oxides.

In our work, the atomistic simulation is used to identify low-energy sites for Li^+ within the β-$AgVO_3$ lattice and to illustrate the migration of interstitial Li^+ for the first time. The calculated structure was generated using the observed structure of β-$AgVO_3$ as a starting point for the energy minimization. Periodic boundary conditions were adopted to optimize cell parameters and atomic positions. As there is limited previous work relating to the atomistic modeling of SVO, the initial approach to simulating the β-$AgVO_3$

(15) Bergstrom, O.; Bjork, H.; Gustafsson, T.; Thomas, J. O. *J. Power Sources* **1999**, *82*, 685.
(16) Nordlinder, S.; Nyholm, L.; Gustafsson, T.; Edstrom, K. *Chem. Mater.* **2006**, *18*, 495.
(17) Kanoh, H.; Tang, W. P.; Ooi, K. *Electrochem. Solid-State Lett.* **1998**, *1*, 17.
(18) Huang, W. W.; Frech, R. *J. Power Sources* **1999**, *82*, 616.
(19) Dokko, K.; Mohamedi, M.; Anzue, N.; Itoh, T.; Uchida, I. *J. Mater. Chem.* **2002**, *12*, 3688.
(20) Itoh, T.; Sato, H.; Nishina, T.; Matue, T.; Uchida, I. *J. Power Sources* **1997**, *68*, 333.
(21) Zhang, X. L.; Frech, R. *J. Electrochem. Soc.* **1998**, *145*, 847.
(22) Baddour-Hadjean, R.; Golabkan, V.; Pereira-Ramos, J. P.; Mantoux, A.; Lincot, D. *J. Raman Spectrosc.* **2002**, *33*, 631.
(23) Inaba, M.; Yoshida, H.; Ogumi, Z.; Abe, T.; Mizutani, Y.; Asano, M. *J. Electrochem. Soc.* **1995**, *142*, 20.
(24) Huang, W. W.; Frech, P. *J. Electrochem. Soc.* **1998**, *145*, 765.
(25) Luo, Y.; Cai, W. B.; Scherson, D. A. *J. Electrochem. Soc.* **2002**, *149*, A1100.
(26) Kalbac, M.; Kavan, L.; Zukalova, M.; Dunsch, L. *Adv. Funct. Mater.* **2005**, *15*, 418.
(27) Kim, Y. A.; Kojima, M.; Muramatsu, H.; Umemoto, S.; Watanabe, T.; Yoshida, K.; Sato, K.; Ikeda, T.; Hayashi, T.; Endo, M.; Terrones, M.; Dresselhaus, M. S. *Small* **2006**, *2*, 667.
(28) Tian, H. J.; Wachs, I. E.; Briand, L. E. *J. Phys. Chem. B* **2005**, *109*, 23491.
(29) Bao, S. J.; Bao, Q. L.; Li, C. M.; Chen, T. P.; Sun, C. Q.; Dong, Z. L.; Gan, Y.; Zhang, J. *Small* **2007**, *3*, 1174.
(30) Gale, J. D. *J. Chem. Soc., Faraday Trans.* **1997**, *93*, 629.
(31) Gale, J. D.; Rohl, A. L. *Mol. Simul.* **2003**, *29*, 291.
(32) Braithwaite, J. S.; Catlow, C. R. A.; Gale, J. D.; Harding, J. H. *Chem. Mater.* **1999**, *11*, 1990.
(33) Olson, C. L.; Nelson, J.; Islam, M. S. *J. Phys. Chem. B* **2006**, *110*, 9995.
(34) Ammundsen, B.; Roziere, J.; Islam, M. S. *J. Phys. Chem. B* **1997**, *101*, 8156.
(35) Ammundsen, B.; Burns, G. R.; Islam, M. S.; Kanoh, H.; Roziere, J. *J. Phys. Chem. B* **1999**, *103*, 5175.
(36) Islam, M. S.; Driscoll, D. J.; Fisher, C. A. J.; Slater, P. R. *Chem. Mater.* **2005**, *17*, 5085.
(37) Mott, N. F.; Littleton, M. J. *Trans. Faraday Soc.* **1938**, *34*, 485.

structure was to use selected, published interatomic potentials. Initial Buckingham parameters for V^{5+}–O potential were taken from the model for V_2O_5 and V_6O_{13},[38,39] Li^+–O parameters were taken from the model for V_2O_5 of Braithwaite et al.,[32] parameters related to Ag were taken from the model of Cleri et al.,[40] and the O–O Buckingham potential and spring constant were from the Lewis[41] library provided by the GULP code. It was found that the best structural reproduction was achieved by using these parameters (listed in Table S1).

The structure of β-$AgVO_3$ was first optimized under constant pressure conditions to obtain the calculated lattice parameters (a = 18.105 914 Å, b = 3.578 682 Å, c = 8.042 99 Å, β = 104.4404°). It was found that the calculated unit cell parameters deviate by less than 0.001 Å from experimental values (listed in Table S2). The simulations show good reproduction which supports the validity of the potentials used for the subsequent defect calculations.

4. Results and Discussion

4.1. Structure Characteristics of β-$AgVO_3$. The typical morphology and microstructure of as-synthesized products have been characterized in our previous work.[28] The products can be indexed to the monoclinic β-$AgVO_3$ with the lattice constants a = 18.1060 Å, b = 3.5787 Å, c = 8.043 Å, and β = 104.44° (space group: *C*2/*m* (No. 12), ICSD No. 56861). Because of lithium insertion, the channel-structured β-$AgVO_3$ loses its crystallinity, resulting in structural changes on the atomic scale. Therefore, it is crucial to understand the structure characteristics of pristine β-$AgVO_3$ before investigating its structure–property relationships and electrochemical behavior.

Rozier et al.[42,43] have determined the structure of β-$AgVO_3$ using XRD and assigned the crystal to the monoclinic system, space group *C*2/*m*, consisting of infinite $[V_4O_{12}]_n$ chains of edge-shared VO_6 octahedra where the chains are zigzag in shape and are double. In fact, the so-called "edge-shared" oxygen atoms are much farther (>2 Å) from the centered V^{5+} than others, and the VO_6 octahedra are highly distorted, resulting in very weak interlayer bond forces. Thus, the V^{5+}-centered pyramids, corresponding to polymeric VO_4^{3-} units, should be the more solid units and more suitable for the studies of structural vibration. Figure 1a shows the three-dimensional packing diagrams of β-$AgVO_3$, where the basic units are V^{5+}-centered tetrahedral that are corner-shared to form undulating chains that align parallel to the *ab*-plane (or along the [010] direction and *b*-axis).

Figure 1b shows the labeling of atoms in two unit cells projected along the [010] direction. There are four types of V sites and four types of Ag sites. Because of the symmetry, the four vanadium atoms are distributed among two types of surroundings, where V1 is the same as V4 and V2 is the same as V3 (shown in Figure S1). V1 (V4) is tetrahedrally coordinated to four oxide ligands: two terminal oxides at short distances of V1–O1 = 1.708 Å and V1–O2 = 1.672 Å and two symmetry bridging oxides at slightly longer distances of V1–O8a = V1–O8b = 1.869 Å to form $[VO_{2/2}O_2]^-$ units. V2 (V3) also has four oxide ligands with different bond lengths from that of V1 (V4): two terminal oxides at short distances of V2–O3 = 1.676 Å and V2–O4 = 1.652 Å and two symmetry bridging oxides at slightly longer distances of V2–O9a = V1–O9b = 1.892 Å to form $[VO_{2/2}O_2]^-$ units. The four silver atoms lay in the mirror plane are distributed among three types of surroundings where Ag2 is equivalent to Ag3 (shown in Figure S1). As described by Rozier et al.,[42] the Ag1 atom is 6-fold-coordinated, locating at the apexes of a regular octahedron; the Ag2 and Ag3 atoms are 5-fold-coordinated with surrounding square-pyramidal oxygen; the Ag4 atom is 7-fold-coordinated in a monocapped trigonal prism.

Two types of channel along *b*-axis with different sizes are formed, which were marked with A and B in Figure 1b. Channel A (surrounded by V4–O11–Ag4–O3″–V2″–O4″–Ag3″) has larger size with the shortest interatom (Ag3″–O3″) distance

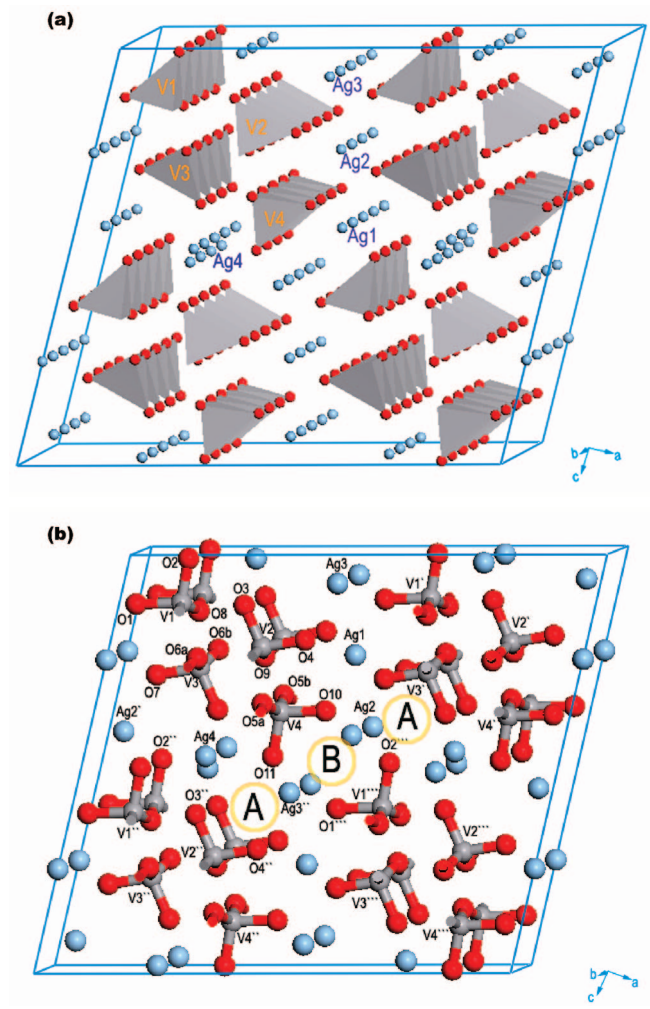

Figure 1. (a) Three-dimensional packing diagrams of β-$AgVO_3$. A 1 × 4 × 2 supercell is generated. (b) Labeling of atoms in two unit cells projected along the [010] direction. Marked A and B in the circles represent two types of channel.

(38) Dietrich, A.; Catlow, C. R. A.; Maigret, B. *Mol. Simul.* **1993**, *11*, 251.
(39) Braithwaite, J. S.; Richard, C.; Catlow, A.; Harding, J. H.; Gale, J. D. *Phys. Chem. Chem. Phys.* **2001**, *3*, 4052.
(40) Cleri, F.; Rosato, V. *Phys. Rev. B* **1993**, *48*, 22.
(41) Lewis, G. V.; Catlow, C. R. A. *J. Phys. C: Solid State Phys.* **1985**, *18*, 1149.
(42) Rozier, P.; Savariault, J. M.; Galy, J. *J. Solid State Chem.* **1996**, *122*, 303.
(43) Rozier, P.; Galy, J. *J. Solid State Chem.* **1997**, *134*, 294.

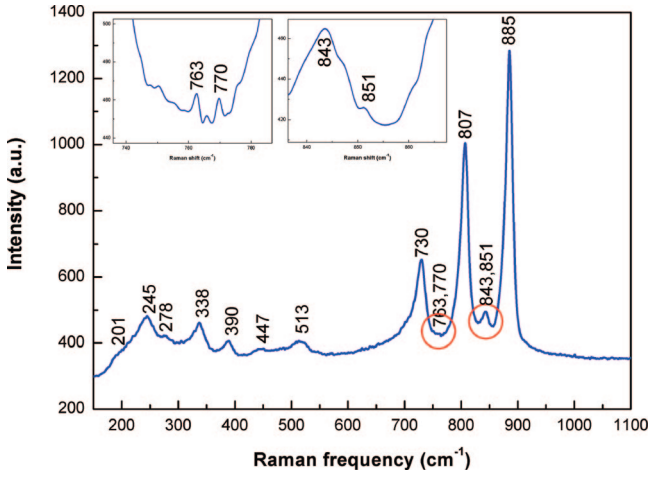

Figure 2. Raman spectrum of as-synthesized β-$AgVO_3$ nanowires. The inset shows the enlarged plot of the red circle.

of 3.658 Å (shown in Figure S2a) in the (*a*, *c*)-plane, which is enough for Li^+ (diameter: 3.12 Å) to migrate freely along the *b*-axis. Channel B (surrounded by V4–O11–Ag3″–O1″–V1″–O2″–Ag2–O10) has symmetric shape with the shortest interatom (Ag2–Ag3′) distance of 3.224 Å (shown in Figure S2b), which might become the "bottleneck" for Li^+ to pass through.

4.2. Raman Spectra of β-$AgVO_3$. Raman vibrational spectra offer capabilities of probing the structure and bonding of a transition-metal oxide complex and thus can be used to discriminate between alternate molecular structures proposed for a given chemical species. Since there is limited previous work relating to the Raman spectrum of crystalline $AgVO_3$, it is necessary to analyze the vibrational modes of crystalline β-$AgVO_3$ and assign the Raman bands of the pristine β-$AgVO_3$ compound.

The β-$AgVO_3$ unit cell consists of eight formula units ($Z = 8$) with 40 atoms in all. In the unit cell of β-$AgVO_3$, all atoms are in the 4*i* positions of the *C*2/*m* space group whereas the Ag_1 is in the 2*c* position. Therefore, one can expect a large number of optically active modes. According to the factor group theory,[44] the total irreducible representation for the vibrational modes of β-$AgVO_3$ is obtained as $\Gamma = 38A_g(xx, yy, zz, xz) + 19B_g(xy, yz) + 21A_u$ (E||*y*) + $42B_u$(E||*x*, E||*z*).

The β-$AgVO_3$ is predicted to show 57 Raman-active modes with $38A_g + 19B_g$ species and 63 infrared-active modes with $21A_u + 42B_u$ species. The free VO_4^{3-} tetrahedron has the T_d point-group symmetry and displays four fundamental vibrational modes: υ_1 (A_{1g}) symmetric stretching; υ_2 (E_g) symmetric deformation; υ_3 (F_2) asymmetric stretching; υ_4 (F_2) asymmetric bending.[45,46]

Figure 2 shows the Raman spectra of as-synthesized β-$AgVO_3$. Typical Raman bands around 201, 245, 278, 338, 390, 447, 513, 730, 763/770, 807, 843/851, and 885 cm^{-1} were observed for all samples. The number of bands observed is only one-quarter of those predicted by a conventional factor group analysis, suggesting great band overlapping. Generally, the short terminal V=O bonds vibrate at the highest frequencies (>800 cm^{-1}); the bridging V–O–V bonds with intermediate length vibrate in the ~500 and 700 cm^{-1} region as symmetric and asymmetric stretching modes; V–O bending modes occur in the 300–400 cm^{-1} region.[47,48] On the basis of the assumption[49,50] that the vibrational interactions between neighboring chemical bonds are neglected, the Raman stretching frequencies can be correlated with the V–O bond length by the empirical expression $\upsilon = 21349 \exp(-1.9176R)$, where υ is the stretching frequency (cm^{-1}) and *R* is the bond length (Å).[49,50] A calculation of the Raman frequency for the VO_4^{3-} tetrahedra using this expression suggests that the internal stretching vibrations exhibit four bands (806, 858, 865, and 899 cm^{-1}) excluding the bridging V−O−V stretching vibrations. This is in good accordance with the experimental observation. Table 1 lists the assignments of the main Raman bands.

The most intense peak at 885 cm^{-1} is assigned to be the stretching vibrations of terminal V=O bonds (V2–O4/V3–O7). Another type of terminal V=O bond (V1–O2/V4–O11) vibrates at a weak Raman band of 851 cm^{-1}. The more intense band at 807 cm^{-1} is assigned to the vibration of symmetric stretching of bridging V–O–V. However, the stretching vibration of the surface atomic oxygen with bridging Ag−O−Ag bonds might also contribute to the strong Raman band at 808 cm^{-1}, which has been demonstrated by isotopic exchange experiments.[51] The asymmetric stretching vibrations of two types of bridging V−O−V bonds (V2−O9a(b)/V3−O6a(b) and V1−O8a(b)/V4−O5a(b)) are also observed at 730 and 763/770 cm^{-1},[28,45] while their symmetric stretching vibrations are observed at 447 and 513 cm^{-1}.[52] The Raman bands at 390 and 338 cm^{-1} are assigned to symmetric and asymmetric deformation modes of the VO_4^{3-} tetrahedron.[53,54] The Raman bands at 278 and 245 cm^{-1} are assigned to asymmetric and symmetric bending modes of the VO_4^{3-} tetrahedron.[28,52] The bands below 200 cm^{-1} are attributed to the external (lattice) modes.

4.3. Electrochemical Measurements. Figure 3 shows the cyclic voltammogram (CV) of the electrodes made from as-synthesized β-$AgVO_3$ in the first cycle at a scan rate of 5 mV/s. The reduction of β-$AgVO_3$ by Li^+ takes place between 3.75 and 1.75 V. Three cathodic peaks (B: 3.45 V; D: 2.8 V; F: 2.25 V) and one anodic peak (H: 2.95 V) were observed from the voltammogram of β-$AgVO_3$. According to ref 8 and constant current discharge experiment (Figure S3), it can be proposed that the Li^+ insertion into β-$AgVO_3$ structure mainly took place by three steps, which correspond to reductions of β-$AgVO_3$.

In order to assign which peak represents silver reduction, the fresh SVO electrodes were discharged to 3.05 V (point C), 2.8 V (point D), 2.55 V (point E), and 2.25V (point F)

(44) Nakamoto, K. *Infrared and Raman Spectra of Inorganic and Coordination Compounds, Part A: Theory and Applications in Inorganic Chemistry*, 5th ed.; John Wiley & Sons: New York, 1997.
(45) Baran, E. J. *J. Raman Spectrosc.* **1997**, *28*, 289.
(46) Benmokhtar, S.; El Jazouli, A.; Chaminade, J. P.; Gravereau, P.; Guillen, F.; de Waal, D. *J. Solid State Chem.* **2004**, *177*, 4175.
(47) Frost, R. L.; Erickson, K. L.; Weier, M. L.; Carmody, O. *Spectrochim. Acta, Part A* **2005**, *61*, 829.
(48) Nordlinder, S.; Lindgren, J.; Gustafsson, T.; Edstrom, K. *J. Electrochem. Soc.* **2003**, *150*, E280.
(49) Brown, I. D.; Wu, K. K. *Acta Crystallogr., Sect. B: Struct. Sci.* **1976**, *B32*, 1957.
(50) Hardcastle, F. D.; Wachs, I. E. *J. Phys. Chem.* **1991**, *95*, 5031.

Table 1. Assignments of Raman Bands of β-$AgVO_3$

bond/unit	bond length (Å)	experimental Raman (cm^{-1})[a]	reference (cm^{-1})[b]	symmetry species	assignment
Ag4−O3	2.216	807 (s)	808	A_g	bridging Ag−O−Ag[51]
V1−O1	1.708	807 (s)	806[cal]	ν_1 (A_{1g})	V−O−Ag
V4−O10					
V1−O2	1.672	851 (w)	865[cal]	ν_1 (A_{1g})	terminal V=O
V4−O11					
V2−O3	1.676	843 (m)	858[cal]	ν_1 (A_{1g})	V−O−Ag
V3−O12					
V2−O4	1.652	885 (s)	899[cal]	ν_1 (A_{1g})	terminal V=O
V3−O7					
V1−O8a(b)	1.869	763, 770 (w)	762, 773	ν_3 (F_2)	asymmetric stretching of bridging V−O−V bonds[28,45]
V4−O5a(b)					
V2−O9a(b)	1.892	730 (s)	738, 737	ν_3 (F_2)	asymmetric stretching of bridging V−O−V bonds[28,45]
V3−O6a(b)					
V1−O8a(b)	1.869	513 (m)	508	ν_1 (A_{1g})	symmetric stretching of bridging V−O−V[52]
V4−O5a(b)					
V2−O9a(b)	1.892	447 (w)	448	ν_1 (A_{1g})	symmetric stretching of bridging V−O−V[52]
V3−O6a(b)					
VO_4^{3-}		390 (m)	366, 365	A_g	symmetric deformation modes of the VO_4^{3-} tetrahedron[53,54]
VO_4^{3-}		338 (m)	324, 330	B_g	asymmetric deformation modes of the VO_4^{3-} tetrahedron[53,54]
VO_4^{3-}		278 (w)	280	ν_4 (F_2)	asymmetric bending modes[28]
VO_4^{3-}		245 (m)	255	B_g	symmetric bending modes[52]
		201 (w)	196, 203		external mode[54]

[a] Relative intensity based on Raman spectrum. s = strong, m = mild, and w = weak. [b] cal: calculation of the Raman frequency based on the empirical expression.[50]

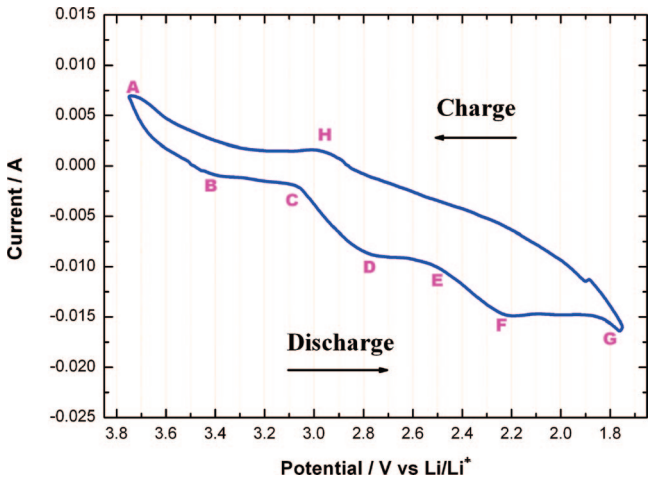

Figure 3. CV curve from the electrode of β-$AgVO_3$ nanowires.

followed by *ex situ* XRD, as shown in Figure 4. The results reveal that the metallic silver is detectable only after the reduction at 2.8 V (point D). This fact confirms that peak D at 2.8 V correlates with the reduction of silver from Ag^+ to Ag^0, and a substitution of Li^+ to Ag^+ occurs from 3.05 V (point C) to 2.55 V (point E). Thus, we can assign the corresponding reduction reactions of three cathodic peaks: the peak B at 3.45 V for the dominant reduction from V^{5+} to V^{4+}, the peak D at 2.8 V for silver reduction from Ag^+ to Ag^0, and the peak F at 2.25 V for reduction of left vanadium from V^{5+} to V^{4+} and for further reduction of vanadium from V^{4+} to V^{3+} and Ag^+ to Ag^0.

4.4. *In Situ* Raman Measurements. Figure 5a,b shows *in situ* Raman spectra of β-$AgVO_3$ nanowires during the cathode reduction process over a potential range from 3.75 to 1.75 V. Apparently, most of the Raman peaks shift to some extent compared to those of the dry power sample shown in Figure 2. Although the confocal Raman spectroscopy was focused onto the sample surface in the measurements, the Raman signals from the solution side species cannot completely be avoided. The Raman bands at 623, 920, and 933 cm^{-1} are obviously correlated with the signal from the electrolyte solution (Figure S4). The Raman bands at 377, 734, and 886 cm^{-1} from the SVO are very close to that from the electrolyte (381, 741, and 878 cm^{-1}), and they are very hard to separate.

In brief, *in situ* Raman spectra could confirm the three lithium insertion steps (A–B–C: 3.55–3.05 V; C–D–E: 3.05–2.55 V; E–F–G: 2.55–1.75 V) that are responsible for the reduction peaks shown on the CV curve. The Raman spectra during the three periods of potential cycling exhibit different features. By analyzing the variation of Raman frequencies corresponding to certain bonds or units, we can distinguish the variations of the local structure and answer these questions: which state of vanadium prefers to be reduced and which silver state would be substituted during the insertion reaction.

In the first lithium insertion step from A to B and C in the CV curve, the inserted Li^+ reduces vanadium from V^{5+} to V^{4+}. The Raman bands at 266, 530, 772, 808, 847, and 886 cm^{-1} vary significantly as a function of potential. These six bands started to be enhanced at 3.35 V and

(51) Wang, C. B.; Deo, G.; Wachs, I. E. *J. Phys. Chem. B* **1999**, *103*, 5645.
(52) Popovic, Z. V.; Konstantinovic, M. J.; Moshchalkov, V. V.; Isobe, M.; Ueda, Y. *J. Phys.: Condens. Matter.* **2003**, *15*, L139.
(53) Yu, J. Q.; Kudo, A. *Adv. Funct. Mater.* **2006**, *16*, 2163.
(54) Gotic, M.; Music, S.; Ivanda, M.; Soufek, M.; Popovic, S. *J. Mol. Struct.* **2005**, *744*, 535.

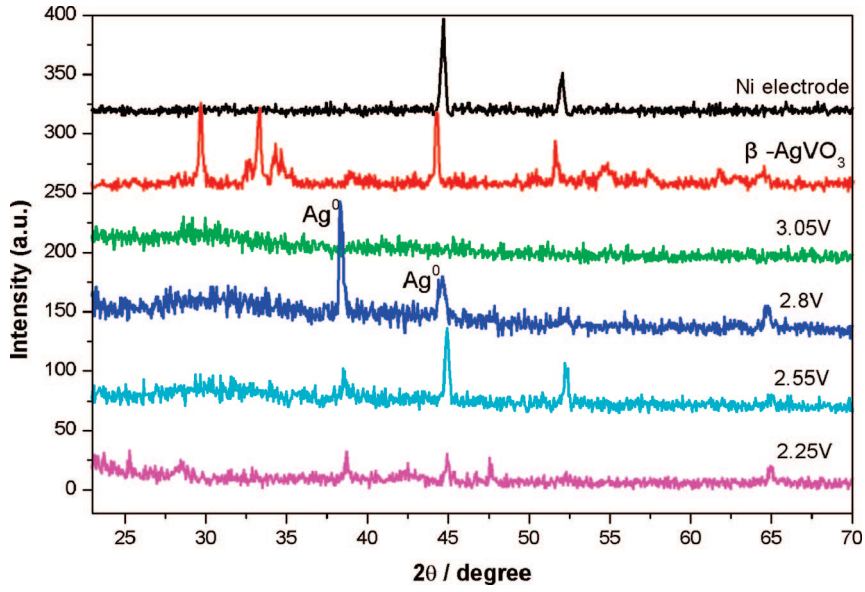

Figure 4. *Ex situ* XRD of β-$AgVO_3$ after reduction to 3.05 V (point C), 2.8 V (point D), 2.55 V (point E), and 2.25 V (point F).

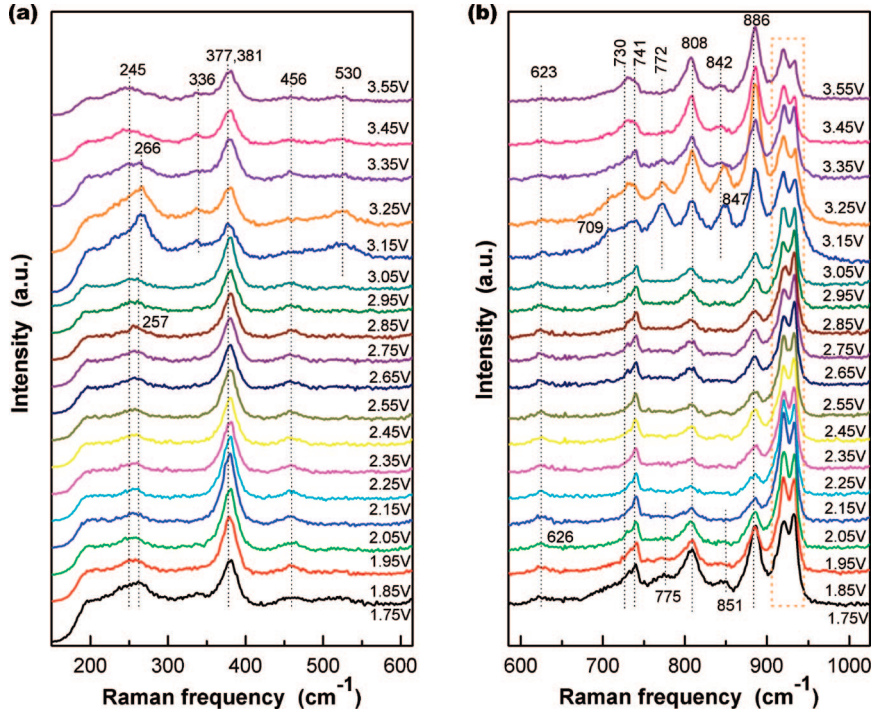

Figure 5. *In situ* Raman spectra of β-$AgVO_3$ nanowires during the lithium insertion. The electrode potential was changed from 3.75 to 1.75 V.

reached the maximum intensity at 3.25 V and then greatly weakened at 3.05 V. In particular, the bands at 772 and 847 cm^{-1} become undetectable at the end of this reduction process (point C, 3.05 V). According to the assignments in Table 1, the Raman frequencies at 513 (shift to 530), 770 (shift to 772), 807 (shift to 808), and 851 (shift to 847) cm^{-1} are originated from the stretching vibration of V–O bonds in V1/V4 pyramids. At the same time, the Raman band at 278 cm^{-1} corresponding to the asymmetric bending modes of VO_4^{3-} pyramids downshifts to 266 cm^{-1} and appears to have a similar dependence on the potential. This might be related to a distorted deformation of the V1/V4 pyramids as lithium enters the host lattice.[22,55] The symmetry of A_{1g} vibrations in the lithiated β-$AgVO_3$ is distorted by the presence of electronic and coordination structures originating from Li–O bonds. Thus, it could be concluded that the inserted Li^+ has great effect on V1/V4 pyramids during the first lithium insertion step and V1/V4 is preferred to be reduced from V^{5+} to V^{4+}.

In contrast, the vibration modes correlated with the V–O bonds in V2/V3 pyramids are partially influenced by the potential variation. The most intense Raman band at 885 (shift to 886) cm^{-1} corresponding to terminal V═O bonds of V2–O4/V3–O7 shows the same dependence on the

(55) Schmitt, T.; Augustsson, A.; Duda, L. C.; Nordgren, J.; Howing, J.; Gustafsson, T. *J. Appl. Phys.* **2004**, *95*, 6444.

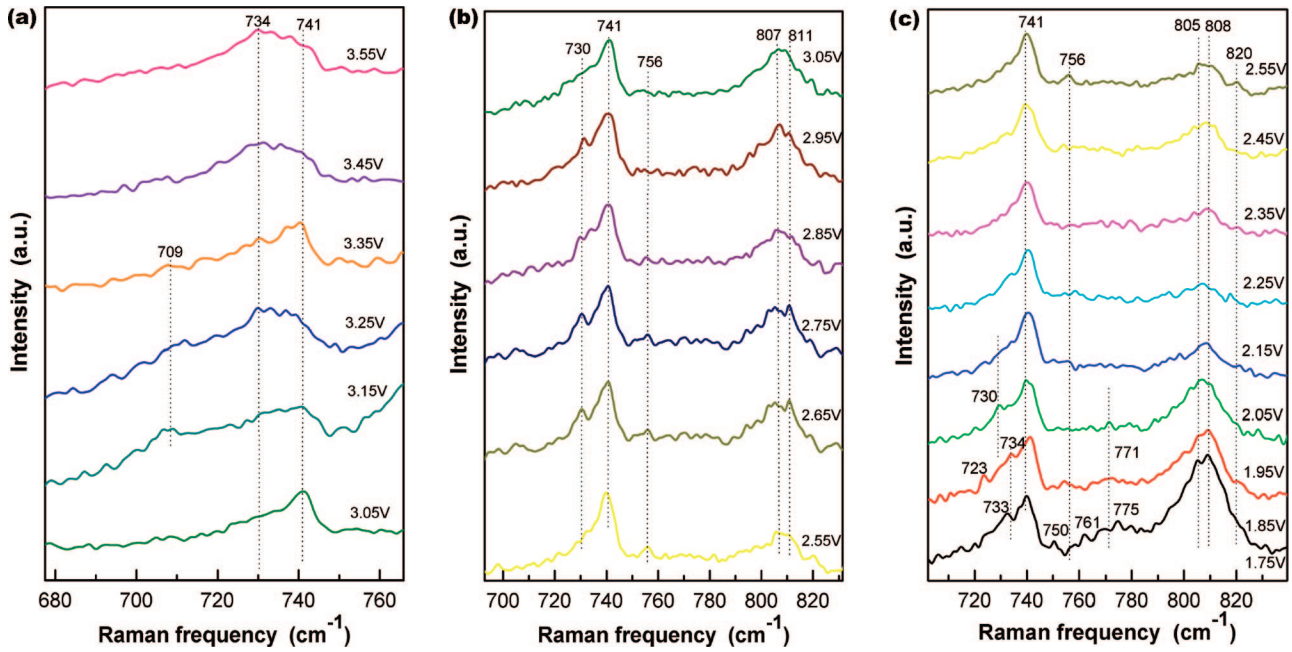

Figure 6. Enlarged Raman spectra of β-$AgVO_3$ nanowires during the cathode reduction. (a) Raman bands between 680 and 760 cm^{-1} while the electrode potential was changed from 3.55 to 3.05 V. (b) Raman bands between 700 and 830 cm^{-1} while the electrode potential was changed from 3.05 to 2.55 V. (c) Raman bands between 700 and 830 cm^{-1} while the electrode potential was changed from 2.55 to 1.85 V.

potential as the discussion above. However, other three types of V–O vibration at 447 (shift to 456), 730 (shift to 734), and 843 (shift to 842) cm^{-1} do not show obvious dependence on the potential. The bands at 734 and 741 cm^{-1} are broadened between 3.35 and 3.05 V and a shoulder band at 709 cm^{-1} appears, as shown by the enlarged Raman spectra in Figure 6a. The bands at 709 and 734 cm^{-1} are decreased at the end of the first reduction step.

In the second lithium insertion step from C to D and E in the CV curve, silver would be reduced and substituted by Li^+. During this step, the Raman intensity is clearly weakened in comparison to the first step. Upon doping with Li^+, the attenuation of Raman spectra can be explained by three main reasons: (1) there exists a loss of the resonance conditions because of charge transfer or a Raman-inactive phase is formed; (2) formation of a solid-electrolyte interphase (SEI)[56,57] film on the surface of SVO electrode causes an abrupt decrease in the intensity at the potential from 3.15 to 3.05 V, where is the end of the first lithium insertion step and the head of the second lithium insertion step; (3) as the potential decreases in the discharge process, the doped Li^+ system gives rise to increased electrical conductivity, resulting in reduction of the optical skin depth.[20]

By a careful inspection of the enlarged Raman spectra in Figure 6b, we can see the Raman spectra do have some small changes. Two Raman bands at 730 and 756 cm^{-1} correlated with the asymmetric stretching of bridging V–O–V bonds appear and become stronger at the end of this step. The variation of these two bands indicates that the unit cell parameter along *b*-axis ([010] direction) changes during the Li insertion process. The Raman band at 741 cm^{-1} most possibly correlated with the electrolyte solution does not show any variation.

The Raman band at 807 cm^{-1} tends to split into two bands at 807 and 811 cm^{-1}. This might indicate the location of Li^+ ions in this reduction step. In this step, Ag^+ is supposed to be reduced and substituted by the inserted Li^+. As Ag4 stays in a monocapped trigonal prism (Figure S1h) surrounded by seven O atoms, we propose that Ag4 is hard to be reduced by Li^+ in the earlier steps, and thus the typical Raman band of Ag4–O3 at 808 (here shift to 807) cm^{-1} is always observed in the whole potential cycling process. The Raman band at 811 cm^{-1} should be originated from the stretching vibration of V1–O1/V4–O10 and the upshift of Raman band is from the shortened V–O bond. Referring to the packing structure shown in Figure 1 and the coordination environment of vanadium shown in Figure S1, it is easy to determine that Li^+ reduced and substituted for Ag2/Ag3 and pressed the surrounded O1/O10 leading to a higher Raman frequency of the V1–O1/V4–O10 stretching bands.

In the third lithium insertion step from E to F and G in the CV curve, further reduction of vanadium (V^{5+}/V^{4+}) and silver would take place. It has been demonstrated that the diffusion of Li^+ ions in vanadium pentoxide nanoribbons is ~3 orders of magnitude faster than that in bulk materials.[58] In our previous work, it has been proved that as produced β-$AgVO_3$ nanowires has much better conductivity than bulk materials.[29] On the basis of these facts, it is very likely that lithium ions are able to diffuse into interior of β-$AgVO_3$ nanowires in this step.

No significant change of the Raman bands at 257, 377/381, 456, 741, 808, and 886 cm^{-1} is observed between 2.55

(56) Gan, H.; Takeuchi, E. S. *J. Power Sources* **1996**, *62*, 45.
(57) Nordlinder, S.; Augustsson, A.; Schmitt, T.; Guo, J. H.; Duda, L. C.; Nordgren, J.; Gustafsson, T.; Edstrom, K. *Chem. Mater.* **2003**, *15*, 3227.
(58) Chan, C. K.; Peng, H. L.; Twesten, R. D.; Jarausch, K.; Zhang, X. F.; Cui, Y. *Nano Lett.* **2007**, *7*, 490.

and 2.05 V, as shown in Figures 5b and 6c. However, these bands tend to be enhanced between 2.05 and 1.75 V, and the Raman spectra show a higher baseline. This could be ascribed to the decrease of the electronic conductivity of β-$AgVO_3$ as most of Ag^+ ions are reduced to Ag^0. The band at 771 cm^{-1} appears at the potential of 2.05 V and shifts to 775 cm^{-1} at the potential between 1.85 and 1.75 V. The band at 756 cm^{-1} appears to split into two bands at 750 and 761 cm^{-1} at the end of this step. As discussed in the second step, the change of these bands suggests the variation of unit cell parameter along the *b*-axis. In addition, the shoulder band at 730 cm^{-1} appears again at the potential of 2.05 V, then splits to two bands at 723 and 734 cm^{-1} at the potential of 1.95 V, and at last these two bands merged into one band at 733 cm^{-1}. This might come from the reduction of vanadium at the site of V2/V3. The further interaction between vanadium at the site of V1/V4 and lithium is also labeled by the split bands at 805 and 851 cm^{-1}. All these variations of Raman bands indicate that more lithium ions are inserted into the host lattice, leading to a significant local structure modification and a crystal lattice distortion in all three dimensions at the end of this step.

4.5. Models of Li^+ Insertion. The above *in situ* Raman studies provide a qualitative analysis of lithium insertion process. By combining with the atomistic simulation, the lowest energy interstitial sites in β-$AgVO_3$ are located and the migration pathways of lithium at the atomic level are confirmed.

The structural parameters optimized from the experimental data (Table S2) were selected as starting point of the computational study. The lowest energy interstitial sites for inserted Li^+ were obtained by placing Li^+ at various positions in the unit cell and allowing the structure to relax. Three main migration steps were considered according to the above discussion. The initial positions of Li^+ of each step in the unit cell were preset as the following: (1) for the first step, Li^+ was put in channel A that has larger "door" size; (2) for the second step, Li^+ substituted Ag2/Ag3; (3) for the third step, Li^+ ions were put at the positions optimized in the first two steps.

The initial positions of Li^+ ions and optimized lowest energy sites are listed in Table S3 and shown in Figure S5. After the optimization, it is concluded that (1) in the first step, Li^+ ions occupy the sites that are very close to Ag2/Ag3 and V1/V4 (Figure S5c,d). This shows good agreement with the *in situ* Raman results, which prove that Li^+ has great effect on V1/V4 pyramids during the first Li^+ insertion step and would prefer to reduce vanadium at these two sites. (2) In the second step, Li^+ ions reduce and replace Ag2/Ag3 and then move to the lowest energy sites that are very close to O1/O10 (Figure S5e,f). This result also confirms the conclusion of *in situ* Raman study, i.e., Li^+ ions press the surrounded O1/O10 after the substitution for Ag2/Ag3. (3) In the third step, the Li^+ ions diffuse to three different sites, one of which stays at the center of the merger channel A and B after the removing of Ag2/Ag3 and the other two stay close to V1/V4 or V2/V3/Ag4 for further reduction (Figure S5g,h). This result is in agreement with the previous assumption in the Raman study.

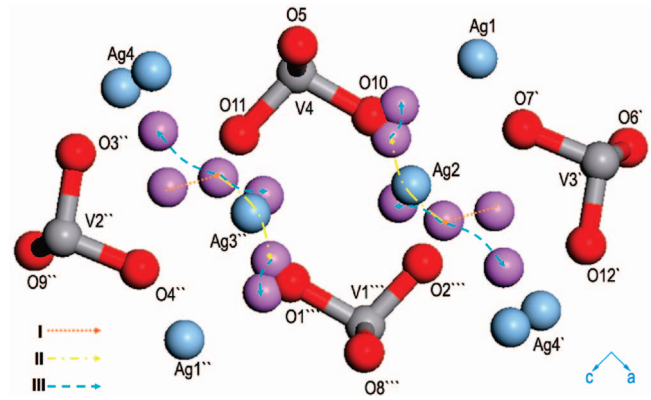

Figure 7. Migration pathways of Li^+ ions in β-$AgVO_3$. Arrows I, II, and III illustrate three lithium insertion steps.

In fact, we found there are more than one lowest energy positions after optimization because there is a flat potential energy surface for Li^+ to move in the channel along *b*-axis.[32] The calculation after each optimization shows that the unit cell parameters along the *a*- and *c*-axis change greatly (Table S4). Therefore, the nature and amplitude of the structural changes induced by Li^+ incorporation depend more on the location of Li^+ ions in the (*a, c*)-plane. Examination of these results reveals migration pathways of lithium ions in the lattice, as shown in Figure 7. Three arrows connecting the initial and final positions illustrate migration pathways of Li^+ ions during the three insertion steps.

5. Conclusions

In conclusion, Raman spectra and structure characteristics of β-$AgVO_3$ nanowires synthesized by a hydrothermal method were studied. Structure changes during lithium ion insertion into β-$AgVO_3$ were investigated using *in situ* Raman spectroscopy. The atomistic simulation was carried to illustrate the migration pathways of Li^+ ions in β-$AgVO_3$. It was found that the lithium insertion can be divided into three steps: (1) Li^+ ions reduce V1/V4; (2) Li^+ ions reduce and substitute Ag2/Ag3; (3) Li^+ ions reduce V2/V3/Ag4 and further reduce V1/V4.

Acknowledgment. This work was jointly supported by the Center for Advanced Bionanosystems of Nanyang Technological University, Singapore, and the Foundation for the Author of National Excellent Doctoral Dissertation of P. R. China (FANEDD No. 200233).

Supporting Information Available: Parameters related to computer simulation, models illustrating channels and coordination environment of V/Ag, discharge curve, Raman spectra of the electrolyte solution, and optimized Li^+ defect positions in β-$AgVO_3$ at each reduction step. This material is available free of charge via the Internet at http://pubs.acs.org.

CM071728I